Origin of metallic ferroelectricity in group-V monolayer black phosphorus

Wen Xu [1], Ya-Ping Shao [1], Jiu-Long Wang,[1] Jun-Ding Zheng [1], Wen-Yi Tong [1,*] and Chun-Gang Duan [1,2,3,†]

[1]*Key Laboratory of Polar Materials and Devices, Ministry of Education, East China Normal University, Shanghai 200241, China*

[2]*Collaborative Innovation Center of Extreme Optics, Shanxi University, Taiyuan, Shanxi 030006, China*

[3]*Shanghai Center of Brain-Inspired Intelligent Materials and Devices, East China Normal University, Shanghai 200241, China*

(Received 3 September 2023; revised 19 December 2023; accepted 20 December 2023; published 17 January 2024)

Recent research has shown that monolayer black phosphorus (BP) can be metallic while sustaining spontaneous polarization. Using density-functional calculations and mean-field theory, we perform a systematic study on the origin of the metallic ferroelectricity in monolayer BP which is composed of only one element with a strong covalent bond. We find that, in contrast to ionic compounds, metallic monolayer BP exhibits lattice deformation between adjacent cells due to the covalent bond. This benefits the survival of spontaneous polarization despite the fact that the long-range Coulomb interactions between dipoles are screened by itinerant electrons. Through the orbital selective external potential method, we reveal that the strength of sp^3 hybridization of monolayer BP significantly impacts such lattice distortion and therefore the ferroelectricity. These findings significantly enrich our understanding of metallic polarization and provide insights to help discover novel ferroelectric materials.

DOI: 10.1103/PhysRevB.109.035421

I. INTRODUCTON

As is well known, ferroelectricity (FE) originates from the delicate balance between short-range elastic forces that favor undistorted paraelectric (PE) structure and long-range Coulomb interactions that promote the FE phase [1]. Itinerant electrons are capable of shielding electric fields, screening out the long-range Coulomb interactions, and thus metallic systems are not expected to display ferroelectriclike structural distortions. However, this traditional view was called into question by the first experimental observation of a structural transition from centrosymmetric to noncentrosymmetric in metallic $LiOsO_3$ [2] at a temperature of $T_s = 140$ K.

In fact, as early as the 1960s, using a phenomenological theory, Anderson and Blount proposed the concept of *ferroelectric metal* and the polar structure possibly appears in certain martensitic transitions involving inversion symmetry breaking [3]. In 2014, Puggioni and Rondinelli proposed the *decoupled electron mechanism* (DEM) model [4], stating that the existence of polar metals relies on weak coupling between the electrons at the Fermi level, and the (soft) phonons are responsible for removing inversion symmetry. This DEM model is later found to be useful in explaining the stability of $LiOsO_3$ [5]. Since then, extensive research has been conducted to analyze the fundamental principles of such materials [6–12]. However, the switching of the polarization in such polar metals remains an unresolved issue in three-dimensional materials, as the itinerant electrons have the ability to shield electric fields.

In recent years, along with the discovery of a large number of two-dimensional (2D) ferroelectric materials (such as $CuInP_2S_6$ [13–15], SnTe [16], SnSe [17], GeSe [18–20], SnS [21], MoS_2 [22,23], and $\alpha - In_2Se_3$ [24–26]), 2D polar metals also emerge, including perovskite oxides [27,28] and $MoTe_2$ [29]. Additionally, it is predicted that monolayer CrN [30] and layered $Bi_5Ti_5O_{17}$ [31] will exhibit ferroelectric metal behavior. Remarkably, two- or three-layered WTe_2 has displayed spontaneous electric polarization that can be manipulated with an external electric field [32,33]. This discovery may be the first experimental proof of the simultaneous existence of both ferroelectricity and metallicity in 2D materials.

In general, 2D ferroelectrics and polar metal [34–37] are compounds composed of different elements and possess ionic bonds. Elementary ferroelectrics—which are composed of only one element with a strong covelent bond, such as As, Sb, and Bi [38,39]—break conventional wisdom and thus have attracted specail research interest. Coincidentally, monolayer black phosphorus (BP), a more famous group-V system with significant advantages in application [40–43], shows the ability to switch between a semiconductor and a metallic state through the strain effect, while still maintaining its spontaneous polarization [44].

In this work, we show that ferroelectricity and metallicity coexist in monolayer BP. Despite the presence of itinerant electrons, there remains structural distortion in monolayer BP that fosters long-range order of local dipoles. Using the mean-field theory, electron doping, and orbital selective external potential (OSEP) methods, we analyze these interactions in metallic monolayer BP. Our research has significant implications for the exploration of metallic ferroelectrics and the search for novel metal ferroelectric materials as it deepens our insight into the mechanism of polar metals.

*wytong@ee.ecnu.edu.cn
†cgduan@clpm.ecnu.edu.cn

II. METHODOLOGY

The calculations were performed within the density-functional theory (DFT) approach in the plane-wave formulation implemented in the Vienna *ab initio* package (VASP) [45]. Local density approximation (LDA) was used for the exchange-correlation functional with a projector augmented-wave pseudopotential (PAW) [46]. The kinetic-energy cutoff of 600 eV is applied to the plane wave expansion and a Γ-centered $7 \times 7 \times 1$ k-point grid is adopted for Brillouin zone sampling. A vacuum space above 20 Å was introduced to avoid interactions between image layers and all the structures are optimized until the Hellmann-Feynman forces are below 1 meV/Å. The convergence threshold of electronic energy is 10^{-5} eV. Lattice dynamics calculations were performed with the PHONOPY package [47]. An $8 \times 8 \times 1$ supercell, sufficiently large for phonon bands to converge was used for calculating the force constant matrices. The spontaneous polarization value polarizations are calculated by the Born effective charge, which has been widely used to simulate polarizations for polar metal systems. Nonadiabatic Born effective charge is more efficient for characterization of polarizability in metals [36], yet beyond the topic here.

The orbital selective external potential (OSEP) method [48], analogous to the LDA+U method, was used to explore the influence of orbital hybridization on the interaction between local electric dipole moments. A projector operator $|inlm\sigma\rangle\langle inlm\sigma|$ that allows the external potential V_{ext} to influence the specific atomic orbital $|inlm\sigma\rangle$ was defined. Here, i denotes the atomic site and n, l, m, σ are the main quantum number, orbital quantum number, magnetic quantum number, and spin index, respectively. The new Hamiltonian can be written in the following form:

$$H^{\text{osep}} = H^{0}_{\text{KS}} + |inlm\sigma\rangle\langle inlm\sigma| V_{\text{ext}} \quad (1)$$

H^{0}_{KS} is the original Kohn-Sham Hamiltonian. Then we solved the new Kohn-Sham equation using the new Hamiltonian H^{osep} in the self-consistent stage. Using this method, the hybridization strength between two atomic orbitals can be easily strengthened or weakened. This method has been successfully applied to study perovskite ruthenates [49], perovskite oxides [50], and europium monochalcogenides [51].

III. RESULTS AND DISCUSSION

There are four atoms in the primitive unit cell of monolayer BP. Due to the strong sp^3-hybridization character of P atoms [38,52], each P atom forms covalent bonds with three adjacent atoms; two of them are in the same plane while the third is in an adjacent plane [Fig. 1(c)]. In the absence of strain, the crystal structure space group of monolayer BP is *Pnma* with central inversion symmetry, which forbids ferroelectricity. When sufficiently large compressive strain is applied, the two originally flat atomic sublayers become buckled with the height difference (h). The band gap of monolayer black phosphorus decreases with the application of compressive strain, and eventually closes [Fig. 1(e)] with a 10% compressive strain, resulting in a metallic state. The monolayer BP with strains of 10%, 11%, and 12% have been selected as

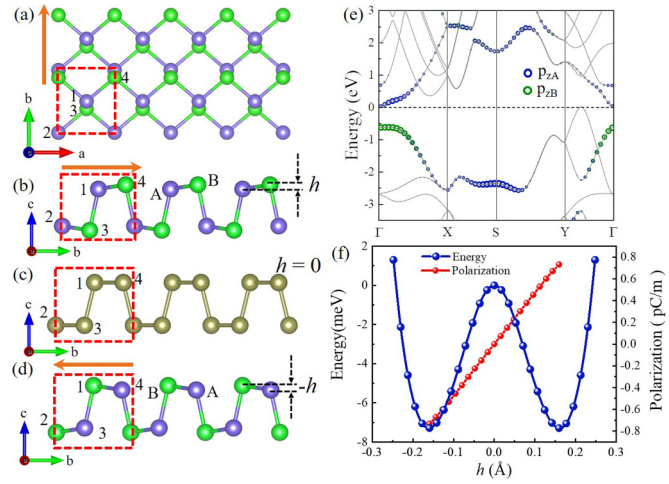

FIG. 1. (a) Top view and (b) side view of polar-distorted (h) monolayer BP. (d) Side view of distorted ($-h$) structure of monolayer BP. The rectangle with red dashed lines indicates the unit cell. The brown arrow indicates the direction of electric dipole moment. The atoms are colored based on the sign of net charge reported in Table S1 [53] (purple for negative and green for positive) and marked with A and B, respectively. (e) Band structure of distorted (h) monolayer BP at 10% compressive strain on the b axis. The size of the blue (green) circles represents the contributions of the p_z orbital of sublattice A (B). (f) Double-well potential of distorted (h) monolayer BP at 10% compressive strain on the b axis. Blue circles are the DFT-calculated total energy and red circles are the spontaneous polarization values under the corresponding structural distortion.

calculation examples. The top view and side view of buckled atomic arrangements are sketched in Figs. 1(a) and 1(b) respectively. It should be noted that there are two sets of sublattices in the crystal structure of the deformed monolayer BP, which are named as A and B. In this deformed $Pmn2_1$ structure, the center inversion symmetry vanishes, enabling the development of ferroelectricity [44]. Interestingly, this spontaneous polarization remains stable under greater compressive strain, even when the band gap is closed. The polarization flips its direction when the lattice distortion h switches to $-h$ as depicted in Fig. 1(d). As shown in Fig. 1(f), almost all phonon modes possess real frequencies throughout the whole Brillouin zone, suggesting that the distorted monolayer BP with closed band gap is still dynamically stable.

The band structure of h-distorted monolayer BP is shown in Fig. 1(e). The conduction band is primarily composed of the p_z orbitals of sublattice A, whereas the valence band is dominated by the p_z orbitals of sublattice B, as illustrated in Fig. 1(e). In contrast to monolayer BP with no wrinkles ($h = 0$ Å), both the valence and conduction bands at the Γ point originate mainly from the p_z orbitals of the p_1 and P_4 atoms (Fig. S1; see the Supplemental Material [53]), indicating that the p_z orbitals in each P atom are degenerate in terms of energy. The h distortion in monolayer BP could result in a net charge transfer between two adjacent P atoms, and therefore lift the degeneracy of the p_z orbitals of P atoms [44] [Fig. 2(c)]. Such charge transfer also leads to spontaneous polarization in monolayer BP. In addition, the A_1 optical branch [depicted in Fig 2(a)] of the phonon spectrum demonstrates an

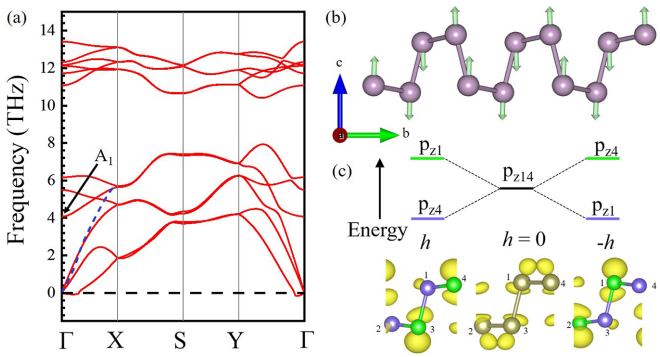

FIG. 2. (a) Phonon spectra related to the distorted (h) structure of monolayer BP at 10% compressive strain. The blue dashed line indicates the A_1 optical branch in the undistorted monolayer BP with 10% compressive strain on the b axis. (b) Phonon eigenvectors of the mode A_1. (c) Illustration of the revolution of p_z orbitals. The partial charge density at the Γ point is shown in the bottom panel.

imaginary frequency in undistorted monolayer BP [Fig 1(c)]. However, it exhibits real frequencies throughout the entire Brillouin zone in a h-distorted black phosphorus structure [as illustrated in Fig 2(b)]. This also supports the stability of the h-distorted (ferroelectric) phase.

To visualize and investigate the interactions between unit cells, we begin by constructing a $4 \times 4 \times 1$ supercell comprising 16 uniformly polarized unit cells with 10% compressive strain. We evaluate the charge density of this supercell, identified as ρ_{FE_0}, and then subsequently switch the polarization of a single cell within the supercell, resulting in 15 cells continuing to exhibit the same polarization (Fig. S3; see the Supplemental Material [53]). The charge density of this modified supercell was then calculated and identified as ρ_{FE_1}. This modification induces a redistribution of charge throughout the supercell, with the response to this local dipole affecting the surrounding cells. The ensuing alteration of charge density, denoted as $\Delta\rho = \rho_{\mathrm{FE}_1} - \rho_{\mathrm{FE}_0}$, offers insight into the interaction between the local dipole and the neighboring cells, as depicted in Figs. 3(a) and 3(b). The switching of the polarization direction of the unit cell induces a flow of electrons in the monolayer BP from the negative to the positive direction of the c axis [Fig. 3(b)]. This flow of electrons aligns with the earlier analysis of the band structure components [Fig. 1(e)]. A part of the charge redistribution region is distributed along the chemical bonds between P atoms, and some of the charge redistribution regions even extend to the sub-nearest-neighboring unit cell [Fig. 3(a)]. This interaction, described as covalent-bond interaction, remains unaffected by the presence of traveling electrons. It should be emphasized that the potency of this interaction hinges on the sp^3 hybridization strength of the P atom, as will be demonstrated later.

The direction of spontaneous polarization in a monolayer BP unit cell is connected to its structural distortion, as illustrated in Figs. 1(b) and 1(d). As such, investigating the possible impact of these covalent-bond interactions on the long-range order of this distortion is crucial; we then changed the structural distortion of these unit cells from h to $-h$, one by one. The energy of these 17 supercells was calculated separately [as shown in Fig. 3(c)]. The supercell exhibiting the highest energy has a split configuration wherein one-half of the internal cell features the h lattice distortion while the other half showcases the $-h$ lattice distortion. It is not unexpected that supercells characterized by a single type of lattice distortion, whether it be h or $-h$, possess the lowest energy levels. This suggests that this covalent-bond interaction between cells can induce long-range structural distortion, resulting in the organization of local dipoles into a long-range order.

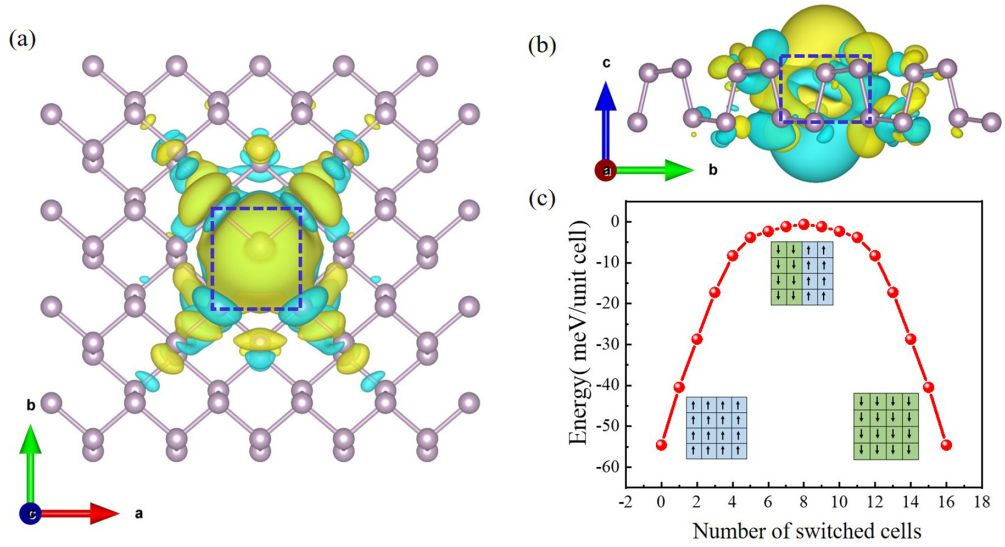

FIG. 3. (a) Top and (b) side view of differential charge density ($\Delta\rho = \rho_{\mathrm{FE}_1} - \rho_{\mathrm{FE}_0}$) diagrams of a $4 \times 4 \times 1$ supercell with 10% compressive strain on the b axis before and after we flip the polarization of one unit cell. Rectangle with blue dashed lines indicates the unit cell where the polarization direction was switched. The area in yellow is the region that gained electrons and the area in green is the region that lost electrons. (c) Energy as a function of the number of switched cells. The direction of the black arrow indicates the direction of spontaneous polarization of the unit cell.

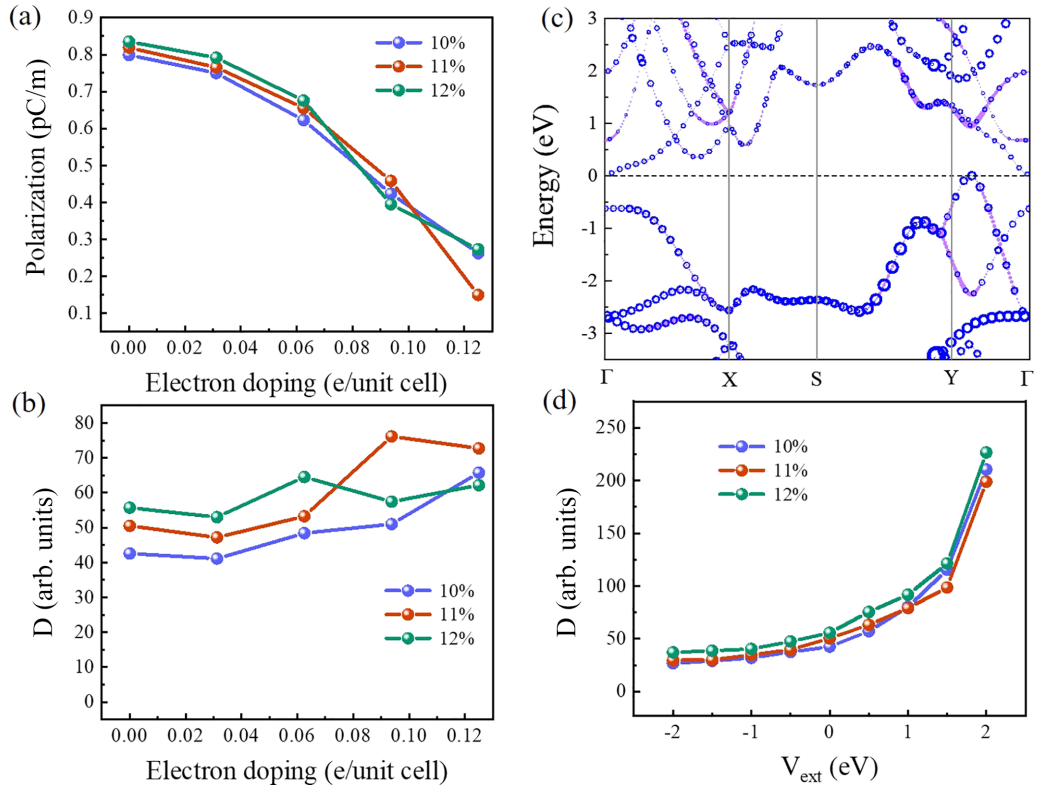

FIG. 4. (a) Spontaneous polarization values and (b) the parameter D as a function of electron doping with compressive strain of 10%, 11%, and 12% on the b axis. (c) Fat band of distorted (h) monolayer BP at 10% compressive strain on the b axis. The size of the purple and blue circles represents the contributions of the s and p orbitals of the P atom, respectively. (d) The parameter D as a function of the variation of s-orbit energy level employing the OSEP method.

Essentially, this type of interaction between cells resembles the long-range Coulomb interactions observed in promoting the FE phase.

This covalent-bond interaction between cells that relates to structural distortion shares similarities with the interaction between local dipoles. In single-layer BP, the magnitude of the spontaneous polarization is directly proportional to the degree of structural distortion, as shown in Fig. 1(f). This correlation allows us to quantify the strength of this interaction between cells by utilizing the D parameter in the Landau-Ginzburg expansion equation [Eq. (2)]. To investigate the influence of itinerant electrons on this covalent-bond interaction between cells, electrostatic doping is employed and we compute the spontaneous polarization and parameter D in Eq. (2) (describing the average covalent-bond interaction between cells) across various electron concentration injection scenarios in a $4 \times 4 \times 1$ supercell, as depicted in Figs. 4(a) and 4(b), respectively. The value of spontaneous polarization in monolayer BP, which exhibits metallic polarization, decreases as the electron doping concentration is increased, eventually dropping to almost zero [Fig. 4(a)]. This indicates the redistribution of itinerant electrons can counterbalance the net electron transfer prompted by the lift of the degeneracy of the P atom's p_z orbital. However, the parameter D exhibits less variation with increasing electron doping concentration [Fig. 4(b)], implying that the itinerant electrons, capable of free movement, do not exert a significant influence on the covalent-bond interaction between cells.

It is well known that the chemical bond between the P atoms in BP is formed through sp^3 hybridization [38,52] [Fig. 4(c)] and the strengths of hybridization between different atomic orbitals are related to the energy difference of the energy levels between them. Here, the OSEP method is employed as a tool to shift the s-orbital energy level of the P atom, thus manipulating the energy difference between the s and p orbitals of the P atom (Fig. S8; see the Supplemental Material [53]). The parameter D in Eq. (2) is still used here to measure the strength of covalent-bond interaction between cells, and the calculation is shown in Fig. 4(d). When the external field V_{ext} is positive, the energy level of the s orbital is shifted up, resulting in a small energy gap between the s and p orbitals, and consequently a stronger sp^3 orbital hybridization in BP (Fig. S8(b); see the Supplemental Material [53]). The parameter D exhibits a rapid increase with the external field strength, and at a field strength of 2 eV, D is five times larger than in the absence of an external field, signifying that the intensity of sp^3 orbital hybridization strength has a significant effect on the covalent-bond interaction between cells. Similarly, when V_{ext} is negative, the energy of the s orbital is shifted down, leading to an enlarged energy gap between the s and p orbitals, and hence, a weakened intensity of sp^3 orbital hybridization (Fig. S8(a), see the Supplemental Material [53]). The value of parameter D decreases with an increase in the external field with negative value, affirming once more that sp^3 orbital hybridization strength has an impact on the covalent-bond interaction between cells.

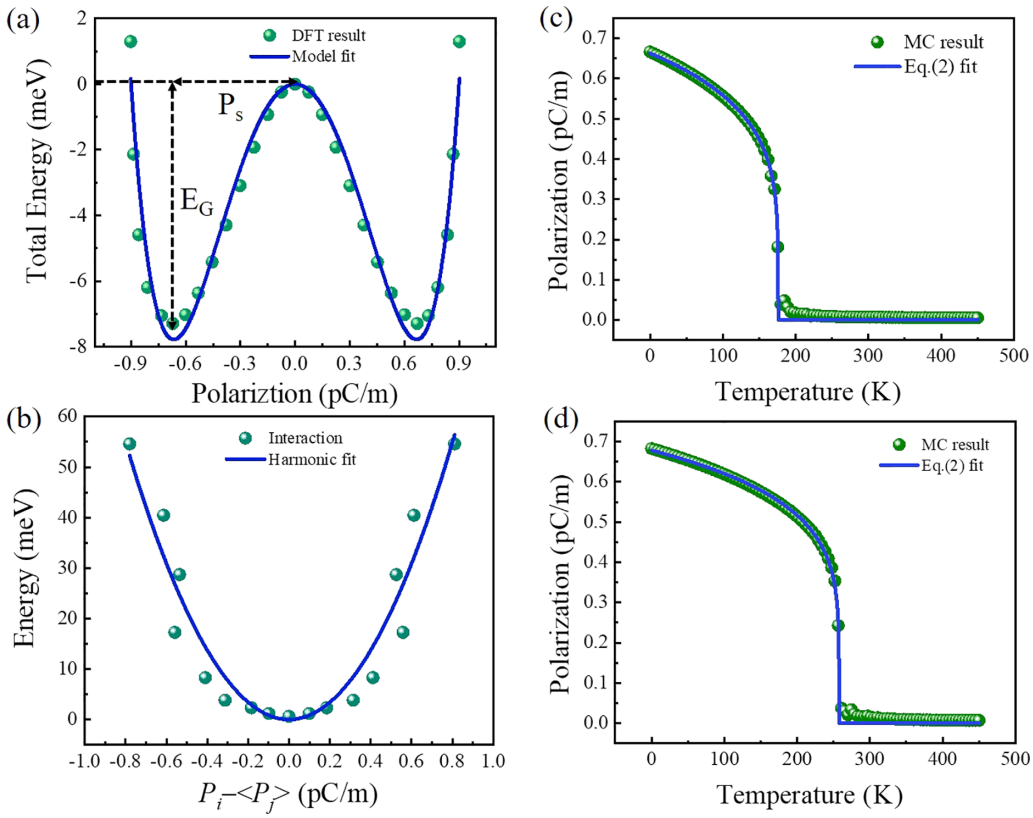

FIG. 5. (a) Double-well potential vs polarization of monolayer BP with 10% compressive strain on the *b* axis. E_G is the ground-state energy (potential barrier) and P_s is the spontaneous polarization. (b) The dipole-dipole interaction of monolayer-distorted (*h*) monolayer BP at 10% compressive strain on the *b* axis using mean-field theory. The green circles are the DFT-calculated total energy of different $P_i\langle P_j\rangle$. The blue line is fitted by the harmonic approximation. Temperature dependence of polarization obtained from MC simulations of distorted (*h*) monolayer BP at (c) 10% compressive strain and (d) 12% compressive strain.

To quantitatively study the interaction between cells and figure out the corresponding temperature related to phase transition, which has been thoroughly researched in other ferroelectric insulating materials [35,54,55], in the following, we build a quantitative approach for exploring the phase transition beyond zero-temperature DFT calculations. We present our system through the Landau theory, wherein the order parameter is the polarization P and is directly linked to the potential energy. The potential energy is expressed in the Landau Ginzburg expansion [54,56,57],

$$E = \sum_i \frac{A}{2}\left(P_i^2\right) + \frac{B}{4}\left(P_i^4\right) + \frac{C}{6}\left(P_i^6\right) + \frac{D}{2}\sum_{\langle i,j\rangle}(P_i - P_j)^2, \quad (2)$$

where i and j label the unit cells and coefficients A, B, and C are associated with the energy contribution from the local modes up to sixth order, describing the anharmonic double-well potential and they can be fitted by DFT calculations, D is describing the average covalent-bond interaction between cells.

Coefficients A, B, and C in the Landau-Ginzburg expansion can be viewed as the Taylor series of local structural distortions with a certain polarization defined at each cell P_i. The coefficients A, B, and C are obtained by fitting the double-well potential vs polarization, calculated by DFT calculations, as depicted in Fig. 5(a). The ground-state energy (potential barrier) and the spontaneous polarization are denoted by E_G and P_s, respectively. Table I presents the values for the parameters A–C, E_G, and P_s. Notably, the magnitude of spontaneous polarization increases when subjected to an increase in compressive strain from 10% to 12%, further emphasizing the impact of strain on spontaneous polarization. Conversely, the potential barrier experienced a nearly twofold increase, rising from 7.75 to 14.69 meV with the same increase in compressive strain. The parameter D is obtained by fitting the DFT-calculated total energy of different $P_i\langle P_j\rangle$ values and is listed in Table I. The first-principles calculations of supercells reveal that the coupling is harmonic [Fig. 5(b)], confirming the soundness of including second-order interactions in Eq. (2). Moreover, it is evident that the interaction

TABLE I. The ground-state free energy (potential barrier) E_G (meV), the spontaneous polarization P_s (pC/m) at zero temperature, and fitted parameters in Eq. (2). A, B, and C are used to describe the double-well potential. D is the constant representing the average covalent-bond interaction between cells.

Strain (%)	E_G	P_s	A	B	C	D
–10	7.75	0.73	–61.03	76.49	137.22	42.58
–11	10.91	0.76	–83.85	107.05	163.46	50.50
–12	14.69	0.78	–105.10	83.11	305.62	55.70

TABLE II. Curie temperature (T_c) and critical exponents in Eq. (2).

Strain (%)	T_c (K)	μ	δ
–10	175.8	0.23	0.20
–11	225.1	0.22	0.20
–12	257.5	0.24	0.19

among cells has a tendency to maintain the orientation of each dipole in a uniform direction, resulting in a long-range ordering of dipoles, owing to the fact that $P_i\langle P_j\rangle = 0$ represents the minimum energy state. It is worth noting that the parameter D, which characterizes the average covalent-bond interaction between cells, shows minimal variation, increasing only from 42.58 to 55.70 as the compressive strain rises from 10% to 12%.

With these parameters, we employ Monte Carlo (MC) simulation to investigate the phase transition. Taking monolayer BP with 10% compressive strain as an example, there is an abrupt transition at temperature 175 K as shown in Fig. 5(c). In order to obtain the critical exponents and gain a better understanding of universal critical phenomena, we utilize a fitting process that operates under the assumption of a heuristically derived form for $P(T)$,

$$P(T) = \begin{cases} \mu(T_c - T)^{\delta} & T < T_c, \\ 0 & T > T_c \end{cases} \tag{3}$$

where T_c is the Curie temperature, δ is the critical exponent, and μ is a constant. The results obtained from fitting monolayer BP with compressive strains of 10%, 11%, and 12% are summarized in Table II. When experiencing a compressive strain range of 10%–12%, parameters μ and δ display negligible variations, consistently measuring at approximately 0.22 and 0.20, respectively. This consistency can be attributed to the fact that, despite altered strain conditions, the phase transition type remains unchanged across the different strain conditions and the value of spontaneous polarization in monolayer BP exhibits minimal fluctuations under increasing compressive strain. With an increase of compressive stress from 10% to 12%, the Curie temperature exhibits a notable rise from 175.81 to 257.5 K, a significant surge of 46%. The phase transition temperature is higher than that of $LiOsO_3$ [2], occurring at 140 K.

In addition, the ability of monolayer BP to switch between a semiconductor and metallic state through strain, while still maintaining its spontaneous polarization, offers a strategy to indirectly reverse the polarization direction of polarized metals. Firstly, the polarization states of metals that are difficult to reverse are converted into a semiconductor polarization state, which can then be reversed through an electric field. Once the material is in a semiconductor state, the polarization direction can be flipped using an electric field. Finally, strain is applied to bring the material back to its original metallic state, successfully reversing the direction of polar metal.

IV. CONCLUSION

In conclusion, we investigate the polarization of metallic monolayer BP, through first-principles calculations. The spontaneous polarization of the metallic state in monolayer BP is a result of the net charge transfer due to the lift of the degeneracy of p_z orbitals of the adjacent P atom. Although the itinerant electrons screened the long-range Coulomb interactions, there remain cell to cell interactions in monolayer BP that foster the long-range order of local dipoles. By employing electrostatic doping, we reveal that the itinerant electrons do not exert a significant influence on the strength of this covalent-bond interaction between cells. Instead, the strength of sp^3 hybridization significantly impacts this covalent-bond interaction between cells in the metal-polarized state of monolayer BP. The temperature related to phase transition of the metal polarization was 175.8, 225.1, and 257.5 K with 10%, 11%, and 12% compressive strain, respectively. The present results hold crucial implications for comprehending the basics of metal polarization and can effectively guide the search for novel materials exhibiting this property.

ACKNOWLEDGMENTS

This work was supported by the National Key Research and Development Program of China (Grants No. 2022YFA1402902 and No. 2021YFA1200700), the NSF of China (Grants No. 12134003 and No. 12304218), Shanghai Science and Technology Innovation Action Plan (Grant No. 21JC1402000), Shanghai Pujiang Program (Grant No. 23PJ1402200), and ECNU Multifunctional Platform for Innovation.

[1] W. Cochran, Adv. Phys. **9**, 387 (1960).
[2] Y. Shi, Y. Guo, X. Wang, A. J. Princep, D. Khalyavin, P. Manuel, Y. Michiue, A. Sato, K. Tsuda, S. Yu, M. Arai, Y. Shirako, M. Akaogi, N. Wang, K. Yamaura, and A. T. Boothroyd, Nat. Mater. **12**, 1024 (2013).
[3] P. W. Anderson and E. I. Blount, Phys. Rev. Lett. **14**, 217 (1965).
[4] D. Puggioni and J. M. Rondinelli, Nat. Commun. **5**, 3432 (2014).
[5] N. J. Laurita, A. Ron, J. Y. Shan, D. Puggioni, N. Z. Koocher, K. Yamaura, Y. Shi, J. M. Rondinelli, and D. Hsieh, Nat. Commun. **10**, 3217 (2019).
[6] Y. Wang, X. Liu, J. D. Burton, S. S. Jaswal, and E. Y. Tsymbal, Phys. Rev. Lett. **109**, 247601 (2012).
[7] H. M. Liu, Y. P. Du, Y. L. Xie, J. M. Liu, C. G. Duan, and X. Wan, Phys. Rev. B **91**, 064104 (2015).
[8] J. S. Zhou, X. Li, J. M. He, J. Chen, and K. Yamaura, Phys. Rev. B **104**, 115130 (2021).
[9] H. J. Zhao, A. Filippetti, C. Escorihuela-Sayalero, P. Delugas, E. Canadell, L. Bellaiche, V. Fiorentini, and J. Íñiguez, Phys. Rev. B **97**, 054107 (2018).
[10] R. E. Cohen, Nature (London) **358**, 136 (1992).
[11] N. A. Hill, J. Phys. Chem. B **104**, 6694 (2000).
[12] T. H. Kim, D. Puggioni, Y. Yuan, L. Xie, H. Zhou, N. Campbell, P. J. Ryan, Y. Choi, J. W. Kim, J. R. Patzner, S. Ryu, J. P. Podkaminer, J. Irwin, Y. Ma, C. J. Fennie, M. S. Rzchowski, X. Q. Pan, V. Gopalan, J. M. Rondinelli, and C. B. Eom, Nature (London) **533**, 68 (2016).

[13] A. Belianinov, Q. He, A. Dziaugys, P. Maksymovych, E. Eliseev, A. Borisevich, A. Morozovska, J. Banys, Y. Vysochanskii, and S. V. Kalinin, Nano Lett. **15**, 3808 (2015).

[14] F. Liu, L. You, K. L. Seyler, X. Li, P. Yu, J. Lin, X. Wang, J. Zhou, H. Wang, H. He, S. T. Pantelides, W. Zhou, P. Sharma, X. Xu, P. M. Ajayan, J. Wang, and Z. Liu, Nat. Commun. **7**, 12357 (2016).

[15] J. D. Zheng, Y. F. Zhao, H. Hu, Y. H. Shen, Y. F. Tan, W. Y. Tong, P. H. Xiang, N. Zhong, F. Y. Yue, and C. G. Duan, J. Phys.: Condens. Matter **34**, 204001 (2022).

[16] K. Chang, J. Liu, H. Lin, N. Wang, K. Zhao, A. Zhang, F. Jin, Y. Zhong, X. Hu, W. Duan, Q. Zhang, L. Fu, Q.-K. Xue, X. Chen, and S.-H. Ji, Science **353**, 274 (2016).

[17] K. Chang, F. Küster, B. J. Miller, J. R. Ji, J. L. Zhang, P. Sessi, S. Barraza Lopez, and S. S. P. Parkin, Nano Lett. **20**, 6590 (2020).

[18] M. Wu and X. C. Zeng, Nano Lett. **16**, 3236 (2016).

[19] X. W. Shen, W. Y. Tong, S. J. Gong, and C. G. Duan, 2D Mater. **5**, 011001 (2018).

[20] J. D. Zheng, Y. F. Zhao, Z. Q. Bao, Y. H. Shen, Z. Guan, N. Zhong, F. Y. Yue, P. H. Xiang, and C. G. Duan, 2D Mater. **9**, 035005 (2022).

[21] N. Higashitarumizu, H. Kawamoto, C. J. Lee, B. H. Lin, F. H. Chu, I. Yonemori, T. Nishimura, K. Wakabayashi, W. H. Chang, and K. Nagashio, Nat. Commun. **11**, 2428 (2020).

[22] L. Li and M. Wu, ACS Nano **11**, 6382 (2017).

[23] L. Yang and M. Wu, Adv. Funct. Mater. **33**, 2301105 (2023).

[24] S. Wan, Y. Li, W. Li, X. Mao, W. Zhu, and H. Zeng, Nanoscale **10**, 14885 (2018).

[25] W. Ding, J. Zhu, Z. Wang, Y. Gao, D. Xiao, Y. Gu, Z. Zhang, and W. Zhu, Nat. Commun. **8**, 14956 (2017).

[26] C. Cui, W.-J. Hu, X. Yan, C. Addiego, W. Gao, Y. Wang, Z. Wang, L. Li, Y. Cheng, P. Li, X. Zhang, H. N. Alshareef, T. Wu, W. Zhu, X. Pan, and L.-J. Li, Nano Lett. **18**, 1253 (2018).

[27] T. Kolodiazhnyi, M. Tachibana, H. Kawaji, J. Hwang, and E. Takayama-Muromachi, Phys. Rev. Lett. **104**, 147602 (2010).

[28] W. X. Zhou, H. J. Wu, J. Zhou, S. W. Zeng, C. J. Li, M. S. Li, R. Guo, J. X. Xiao, Z. Huang, W. M. Lv, K. Han, P. Yang, C. G. Li, Z. S. Lim, H. Wang, Y. Zhang, S. J. Chua, K. Y. Zeng, T. Venkatesan, J. S. Chen *et al.*, Commun. Phys. **2**, 125 (2019).

[29] H. Sakai, K. Ikeura, M. S. Bahramy, N. Ogawa, D. Hashizume, J. Fujioka, Y. Tokura, and S. Ishiwata, Sci. Adv. **2**, e1601378 (2016).

[30] W. Luo, K. Xu, and H. Xiang, Phys. Rev. B **96**, 235415 (2017).

[31] A. Filippetti, V. Fiorentini, F. Ricci, P. Delugas, and J. Íñiguez, Nat. Commun. **7**, 11211 (2016).

[32] Z. Fei, W. Zhao, T. A. Palomaki, B. Sun, M. K. Miller, Z. Zhao, J. Yan, X. Xu, and D. H. Cobden, Nature (London) **560**, 336 (2018).

[33] P. Sharma, F. X. Xiang, D. F. Shao, D. Zhang, E. Y. Tsymbal, A. R. Hamilton, and J. Seidel, Sci. Adv. **5**, eaax5080 (2019).

[34] W. X. Zhou and A. Ariando, Jpn. J. Appl. Phys. **59**, SI0802 (2020).

[35] X. Y. Ma, H. Y. Lyu, K. R. Hao, Y. M. Zhao, X. Qian, Q. B. Yan, and G. Su, Sci. Bull. **66**, 233 (2021).

[36] C. E. Dreyer, S. Coh, and M. Stengel, Phys. Rev. Lett. **128**, 095901 (2022).

[37] D. Hickox-Young, D. Puggioni, and J. M. Rondinelli, Phys. Rev. Mater. **7**, 010301 (2023).

[38] C. Xiao, F. Wang, S. A. Yang, Y. Lu, Y. Feng, and S. Zhang, Adv. Funct. Mater. **28**, 1707383 (2018).

[39] J. Gou, H. Bai, X. Zhang, Y. L. Huang, S. Duan, A. Ariando, S. A. Yang, L. Chen, Y. Lu, and A. T. S. Wee, Nature (London) **617**, 67 (2023).

[40] M. Galluzzi, Y. Zhang, and X.-F. Yu, J. Appl. Phys. **128**, 230903 (2020).

[41] M. B. Erande, M. S. Pawar, and D. J. Late, ACS Appl. Mater. Inter. **8**, 11548 (2016).

[42] A. N. Abbas, B. Liu, L. Chen, Y. Ma, S. Cong, N. Aroonyadet, M. Köpf, T. Nilges, and C. Zhou, ACS Nano **9**, 5618 (2015).

[43] C. C. Mayorga-Martinez, N. Mohamad Latiff, A. Y. S. Eng, Z. Sofer, and M. Pumera, Anal. Chem. **88**, 10074 (2016).

[44] W. Xu, J. D. Zheng, W. Y. Tong, J. L. Wang, Y. P. Shao, Y. K. Zhang, Y. F. Tan, and C. G. Duan, Adv. Quantum Technol. **6**, 2200169 (2023).

[45] G. Kresse and J. Hafner, Phys. Rev. B **47**, 558 (1993).

[46] P. E. Blöchl, Phys. Rev. B **50**, 17953 (1994).

[47] A. Togo and I. Tanaka, Scr. Mater. **108**, 1 (2015).

[48] Y. Du, H.-C. Ding, L. Sheng, S. Y. Savrasov, X. Wan, and C.-G. Duan, J. Phys.: Condens. Matter **26**, 025503 (2014).

[49] X. Wan, J. Zhou, and J. Dong, Europhys. Lett. **92**, 57007 (2010).

[50] Y. Shen, J. Cai, H. C. Ding, X. W. Shen, Y. W. Fang, W. Y. Tong, X. G. Wan, Q. Zhao, and C. G. Duan, Adv. Theory Simul. **2**, 1900029 (2019).

[51] X. Wan, J. Dong, and S. Y. Savrasov, Phys. Rev. B **83**, 205201 (2011).

[52] Y. Aierken, D. Çakır, C. Sevik, and F. M. Peeters, Phys. Rev. B **92**, 081408(R) (2015).

[53] See Supplemental Material at http://link.aps.org/supplemental/10.1103/PhysRevB.109.035421 for band structures; phonon spectra; double-well and Monte Carlo simulations under other strain conditions, except for 10% strain; and partial density of states (PDOS) of monolayer BP with the orbital selective external potential (OSEP) method.

[54] R. Fei, W. Kang, and L. Yang, Phys. Rev. Lett. **117**, 097601 (2016).

[55] I. C. Infante, J. Juraszek, S. Fusil, B. Dupé, P. Gemeiner, O. Diéguez, F. Pailloux, S. Jouen, E. Jacquet, G. Geneste, J. Pacaud, J. Íñiguez, L. Bellaiche, A. Barthélémy, B. Dkhil, and M. Bibes, Phys. Rev. Lett. **107**, 237601 (2011).

[56] M. D. Glinchuk and A. N. Morozovska, J. Phys.: Condens. Matter **16**, 3517 (2004).

[57] C.-G. Duan, R. F. Sabirianov, W.-N. Mei, S. S. Jaswal, and E. Y. Tsymbal, Nano Lett. **6**, 483 (2006).